Ultrasound in Med. & Biol., Vol. 29, No. 12, pp. 1715–1723, 2003

0301-5629/03/$–see front matter

ELSEVIER

doi:10.1016/j.ultrasmedbio.2003.08.008

● *Original Contribution*

SHEAR-WAVE GENERATION USING ACOUSTIC RADIATION FORCE: *IN VIVO* AND *EX VIVO* RESULTS

KATHRYN NIGHTINGALE,* STEPHEN MCALEAVEY* and GREGG TRAHEY*†
*Department of Biomedical Engineering, and †Department of Radiology, Medical Center, Duke University, Durham, NC, USA

(*Received* 5 *March* 2003; *revised* 7 *July* 2003; *in final form* 8 *August* 2003.)

Abstract—Acoustic radiation force impulse (ARFI) imaging involves the mechanical excitation of tissue using localized, impulsive radiation force. This results in shear-wave propagation away from the region of excitation. Using a single diagnostic transducer on a modified commercial ultrasound (US) scanner with conventional beam-forming architecture, repeated excitations with multiple look directions facilitate imaging shear-wave propagation. Direct inversion methods are then applied to estimate the associated Young's modulus. Shear-wave images are generated in tissue-mimicking phantoms, *ex vivo* human breast tissue and *in vivo* in the human abdomen. Mean Young's modulus values of between 3.8 and 5.6 kPa, 11.7 kPa and 14.0 kPa were estimated for fat, fibroadenoma and skin, respectively. Reasonable agreement is demonstrated between structures in matched B-mode and reconstructed modulus images. Although the relatively small magnitude of the displacement data presents some challenges, the reconstructions suggest the clinical feasibility of radiation force induced shear-wave imaging. (E-mail: kathy.nightingale@duke.edu) © **2003 World Federation for Ultrasound in Medicine & Biology.**

Key Words: **Acoustic radiation force, Remote palpation, Shear-wave imaging, Ultrasound, Sonoelasticity, Acoustic radiation force impulse imaging, Shear modulus, Young's modulus, Soft tissue.**

INTRODUCTION

The ability to image the mechanical properties of tissue noninvasively does not exist commercially today. However, manual palpation of tissues for the purpose of disease identification and diagnosis is regularly performed by clinicians. The utility of manual palpation is limited to more superficial and/or larger structures because deeper and smaller structures are generally obscured by overlying tissues. Thus, the goal of developing an imaging system capable of evaluating the mechanical properties of tissues at depth and with high resolution is being pursued by several researchers (for example: Plewes et al. 2000; Muthupillai et al. 1995; Ophir et al. 1999; Taylor et al. 2000; Hall et al. 2002; Zhu et al. 1999; Sarvazyan et al. 1998; Nightingale et al. 2002b; Walker et al. 2000; Sandrin et al. 2002; de Korte and vander Steen 2002; Steele et al. 2000; McKnight et al. 2002).

Address correspondence to: Kathryn Nightingale, Dept. Biomedical Engineering, Duke University, Box 90281, Durham, NC 27708 0281 USA. E-mail: kathy.nightingale@duke.edu

Methods for imaging the mechanical properties of tissues involve mechanical excitation of the tissue and observation of the tissue response. The traditional types of excitation are static compression (*i.e.,* elastography and strain imaging [Ophir et al. 1999; Steele et al. 2000; Bilgen and Insana 1998; Hall et al. 2002] and quasistatic magnetic resonance elastography (MRE) [Plewes et al. 2000], and dynamic vibration excitation (*i.e.,* sonoelasticity [Taylor et al. 2000; Fu et al. 2000] and dynamic MRE [McKnight et al. 2002; Van Houten et al. 2000; Oliphant et al. 2001; Sinkus et al. 2000]). Transient elastography has also been implemented utilizing transient dynamic excitation to characterize the mechanical properties of tissues (Sandrin et al. 2002). Traditionally, the source of the excitation has been external to the tissue; however, naturally occurring physiologic motion has also been utilized for arterial imaging (Arnett et al. 1994) and for cardiac (D'hooge et al. 2002; Varghese et al. 2003) and arterial strain imaging (de Korte and vander Steen 2002; Mai et al. 2001).

Recently, acoustic radiation force has been used to generate internal mechanical excitation noninvasively (Sugimoto et al. 1990; Sarvazyan et al. 1998; Fatemi and

Greenleaf 2000; Walker et al. 2000; Nightingale et al. 2002b; Bercoff et al. 2002). Acoustic radiation force is generated by a transfer of momentum from the acoustic wave to the tissue. In soft tissues, the force is applied in the direction of wave propagation and the magnitude of the force can be approximated by:

$$F = \frac{W_{absorbed}}{c} = \frac{2\alpha I}{c}, \quad (1)$$

where F, dyn/(1000 cm)^3 or kg/(s^{2}cm^2), is acoustic radiation force, W_{absorbed}, W/(100 cm)^3, is the power absorbed by the medium at a given spatial location, c (m/s) is the speed of sound in the medium, α (Np/m) is the absorption coefficient of the medium and I (W/cm^2) is the temporal average intensity at a given spatial location. The spatial distribution of the radiation force field is, thus, determined by both the transmitted acoustic parameters and the tissue properties. For a thorough discussion of the radiation force phenomenon, the reader is referred to Sarvazyan et al. (1998).

When radiation force is applied to a given spatial volume for a short duration (*i.e.*, the focal region of a focused acoustic beam with a temporal application time on the order of 1 ms), transient shear waves are generated that propagate away from the initial region of excitation (Sarvazyan et al. 1998). Shear-wave propagation speed and attenuation are directly related to the mechanical properties of the tissue. Existing reconstruction methods that derive shear modulus from dynamic displacement information can be applied to these data (Muthupillai et al. 1995; Sinkus et al. 2000; Oliphant et al. 2001; Sandrin et al. 2002; Fu et al. 2000; Bercoff et al. 2002).

Shear modulus reconstruction methods can be divided into two general categories: 1. forward/iterative methods that minimize the difference between displacements calculated using finite element methods with assumed material properties and the experimentally measured displacements (Plewes et al. 2000; Van Houten et al. 2000), 2. direct inversion of the differential equation of motion (Oliphant et al. 2001; Sandrin et al. 2002; Bercoff et al. 2002) can be employed to compute shear modulus. After the shear modulus has been determined, the corresponding Young's modulus can be estimated. The relationships between shear-wave speed, shear modulus and Young's modulus for a linear isotropic medium are provided below:

$$c_t = \sqrt{\frac{\mu}{\rho}}; \mu = G = \frac{E}{2(1+\nu)}, \quad (2)$$

where c_t is shear wave speed, μ is a lame constant, ρ is density, G is shear modulus, E is Young's modulus and ν is Poisson's ratio (which is generally assumed to be 0.5 for soft tissue (*i.e.*, incompressible), providing the relationship $E = 3G$). The second method is considerably less computationally intensive; however, it suffers from limitations when applied to data with poor signal-to-noise ratio (SNR). Forward/iterative methods are more robust in the presence of noise; however, they require knowledge of the tissue structure (*i.e.*, boundary conditions). Recently, the direct inversion method of Oliphant et al. (2001) was applied to radiation-force-induced shear waves in tissue-mimicking phantoms with good results (Bercoff et al. 2002). In this paper, we also employ this reconstruction approach.

Reconstruction of the tissue shear modulus distribution from transient shear-wave excitation as generated using acoustic radiation force is complicated by the fact that frame rates must be fast enough to sample the region-of-interest (ROI) at the Nyquist sampling limit. This can be accomplished in ultrasonography either by extensive parallel processing (Sandrin et al. 2002; Bercoff et al. 2002), which requires custom beam forming architecture, or by repeated interrogations with different "track" directions (which can be implemented on commercial scanners with reduced frame rates), or some combination of the two. In this study, we used the repeated interrogation approach.

The goal of this work was to present preliminary results demonstrating the feasibility of using acoustic radiation force to generate transient shear waves *in vivo* and *ex vivo* and to evaluate the potential for using direct inversion methods to reconstruct shear modulus maps from these data.

METHODS

Experiments were performed in tissue-mimicking phantoms, *in vivo* and in fresh *ex vivo* tissue samples, immediately after surgical excision and prior to pathologic examination. The *in vivo* experiments were performed with a hand-held transducer and a 10-mm standoff pad was placed between the transducer and the skin. The *ex vivo* tissue experiments were performed with the transducer held by a ring stand, these tissues were imaged at room temperature within 2 h of excision. The transducer was coupled to the tissue samples using ultrasonic gel. After imaging the *ex vivo* tissue samples, the location of the transducer was marked with ink and the tissue was dissected along the imaging plane to identify tissue structures corresponding to the ARFI datasets.

Experiments were performed with a Siemens Elegra scanner (Siemens Medical Systems, Ultrasound Group, Issaquah, WA, USA) that has been modified to allow user control of the acoustic beam sequences and intensities, as well as providing access to the raw radiofre-

quency (RF) data. The beam sequences used for these experiments consist of tracking beams and pushing beams. The tracking beams were similar to those transmitted during conventional B-mode imaging; 7.2 MHz, 0.2 μs pulse length, f/1 focal configuration, mechanical index (MI) of 0.4, spatial peak temporal average ($I_{spta.3}$) of 0.1 W/cm^2 and a pulse-repetition frequency (PRF) of 5.6 kHz. Dynamic receive focusing was applied with an f/1 receive aperture. The pushing beams were similar to those transmitted during color Doppler sequences; however, the pulse length was increased considerably and the aperture was not apodized (7.2 MHz, 27.8 μs pulse length, MI of 1.2, $I_{spta.3}$ of $\sim$ 1000 W/cm^2 (applied for less than 1 ms) and a PRF of 5.6 kHz). The total number of pushing pulses (*i.e.,* the duration of high-intensity insonification), aperture size and focal point were varied for different tissues.

The beam sequence was designed to quantify displacement through time throughout a 2-D ROI, keeping the pushing location constant within the ROI. For each series of pushing pulses, a tracking line was fired first, then between two and six pushing lines interspersed with tracking lines (up to 1 ms), followed by several tracking lines to observe the recovery response of the tissue (up to 10 ms). The pushing pulse location remained the same and the location of the tracking lines was sequenced across the ROI, interrogating each location for up to 10 ms. The lateral spacing of the tracking lines was determined by the desired ROI size, and typically ranging from 0.2 to 0.75 mm. After firing the custom pulse sequence, the corresponding B-mode image frame was acquired. Data were acquired in real-time and processed off-line.

The RF echo data (which was obtained by applying depth-dependent focal delays to the data received at each active element and summing these data) were 16-bit data, acquired from the Elegra scanner at a sampling rate of 36 MHz. Off-line data processing was accomplished by performing 1-D cross-correlation in the axial dimension between up-sampled sequentially acquired tracking lines (Trahey et al. 1987; O'Donnell et al. 1994). The RF data were up-sampled to 216 MHz, then each tracking line was divided into a series of search regions 0.53 mm in length; the location of the peak in the cross-correlation function between a kernel in the first tracking line (0.27 mm in length) and the corresponding search region in the next tracking line was used to estimate the axial tissue displacement in that region. Prior to peak location, the correlated signal was further up-sampled to 4.3 GHz. Thus, given an assumed acoustic velocity of 1540 m/s, the minimum measured displacement is 0.18 μm. The up-sampling was performed using a symmetrical filter that allows the original data to pass through unchanged and the interpolated values are selected to minimize the mean square error between them and their ideal values (*i.e.,* the "interp" function in MATLAB). A 75% overlap of the kernel regions was used.

Complete ARFI datasets are generated by combining the data from each interrogation at each time step (1/5632 s). This results in a 3-D data set of 2-D displacement maps (axial and lateral position) that are updated at a rate of 5632 Hz (*i.e.,* a virtual frame rate of 5632 Hz). The *in vivo* data are then filtered to remove the linear component of the temporal profile of the displacement data at each pixel (to account for respiratory and cardiac motion artefacts) (Nightingale et al. 2002b). ARFI data are presented in several ways. Typically, ARFI displacement images are superimposed over matched B-mode images.

To visualize shear-wave propagation, images are generated of axial displacement as a function of lateral position and time at a given depth. In these images, shear-wave speed is reflected by the slope of the leading edge of the wavefront through time. Shear waves are rapidly attenuated in tissue-like media; thus, normalization of the displacement values at each time step allows better visualization of the wavefront.

To quantify the tissue mechanical properties, propagation of the shear wave is modeled by the Helmholtz wave equation (Sandrin et al. 2002),

$$\rho \frac{\delta^2 \vec{u}_i(\vec{x})}{\delta t^2} = \mu \vec{\nabla}^2 \vec{u}_i(\vec{x}), \tag{3}$$

where $\vec{u}_i(\vec{x})$ is the displacement in the i direction at location $\vec{x}$, ρ is density, μ is shear modulus and t is time. This equation applies to each component of displacement independently. Knowledge of a single component (*e.g.,* the z-component) of displacement allows reconstruction of the local shear modulus μ if ρ is assumed constant. The local shear modulus is simply the ratio:

$$\frac{\rho \dfrac{\delta^2 \vec{u}_i(\vec{x})}{\delta t^2}}{\vec{\nabla}^2 \vec{u}_i(\vec{x})} = \mu(\vec{x}) \tag{4}$$

Evaluation of eqn (4) is complicated by noise, the uncertain location of the shear wave and sampling nonuniformity.

The 2-D RF data set allows displacement to be calculated in the z direction with great precision. Calculation of the Laplacian requires knowledge of the z component of $\vec{u}$ in a volume about the location of interest. The partial derivatives of $\vec{u}$ are readily calculated from the displacement map in the z and, with less precision, the x directions. The y component is unknown, however, and here taken to be zero. Outliers in the

displacement data are removed by a median filter. The data are then smoothed by a 2-D Gaussian low-pass filter (Oliphant et al. 2001). From these smoothed displacement estimates, the Laplacian and second temporal derivative are calculated.

If displacement estimates are available at multiple times during the passage of the shear wave for a location of interest in the object, estimates of μ can be calculated at each time step and averaged, as was done here.

A meaningful estimate of μ can only be found if a shear wave is present at the location of interest. Furthermore, inclusion of estimates of μ in the average should depend on the confidence in the estimate. To this end, only estimates of μ for which the denominator term $\vec{\nabla}^2 u_z(x)$ exceeds a threshold are included in the average. The threshold serves the dual purpose of detecting the passage of a shear wave through the ROI, as well as excluding particularly small values of $\vec{\nabla}^2 u_z(x)$ near zero crossings, which are especially noise-sensitive in the denominator. The threshold value (3% of the peak Laplacian value occuring within the data) was determined empirically. Figure 1 provides a flow chart of the calculation. The resulting images of shear modulus are median filtered.

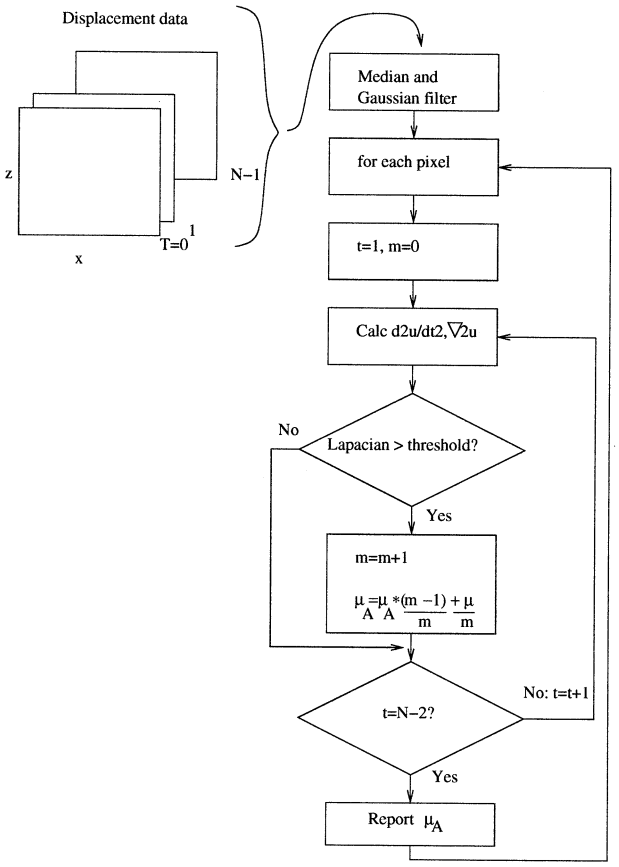

Fig. 1. Flow chart of modulus calculation, showing thresholding on Laplacian.

RESULTS

Two gelatin/graphite phantoms (A and C) with different gelatin bloom strengths (ratio 1:3), were constructed to evaluate the potential for radiation-force-based shear modulus estimation (and, given that the phantoms are relatively incompressible and isotropic, Young's modulus estimation). Given this construction, it is expected that phantom C has a Young's modulus (and shear modulus) that is 3 times greater than phantom A (Hall et al. 1997).

One method for shear-wave propagation visualization is to observe the temporally/varying axial displacement of the tissue at a given depth. For example, at the focal depth, where the region of excitation is the narrowest, shear waves are observed propagating laterally away from the region of excitation through time in phantoms A and C (Fig. 2). The shear-wave speed, which is reflected by the slope of the leading edge of the wave through time, is dependent upon the shear modulus of the phantom; the faster the speed, the higher the shear modulus. The speeds of the wavefronts in the softer phantom (A) (left and middle, Fig. 2) and stiffer phantom (C) (right-hand image, Fig. 2) are estimated to be 1.0 and 1.7 m/s, respectively, corresponding to shear modulus values of 1.0 and 2.9 kPa and Young's modulus values of 3.0 and 8.7 kPa, eqn (2).

In addition to evaluating the shear-wave speed at the focus using the edge of the wavefront in Fig. 2, direct inversion methods were employed throughout the ROI (eqn (4)) to estimate the shear moduli and related Young's moduli, using an assumed Poisson's ratio of 0.5 (Fig. 3). This figure portrays reconstructions in phantoms A and C generated using two different focal configurations. In these reconstructions of homogeneous phantoms, the region of excitation (ROE) is clearly apparent as a region of increased magnitude. The corresponding ROEs are reflected by the 2-D ARFI displacement profiles immediately after force cessation, shown in the first column of Fig. 2. The mean Young's modulus estimates outside of the ROE (within the ROIs indicated on the images) in the different reconstructions are 2.8 $\pm$ 0.5 kPa (upper center, phantom A, f/1.3), 3.8 $\pm$ 0.8 kPa (lower center, phantom A, f/9, weakly focused beam), 6.9 $\pm$ 1.7 kPa (upper right, phantom C, f/1.3) and 10.0 $\pm$ 0.9 kPa (lower right, phantom C, f/9, weakly focused beam). The estimated modulus values are consistently higher for the weakly focused beam.

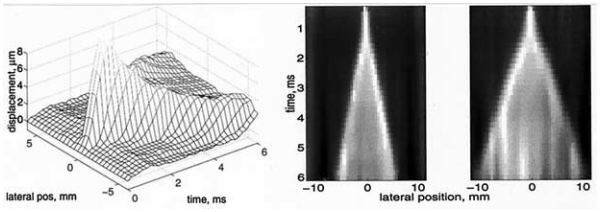

Fig. 2. (Left) Displacement through time at the focal depth (20 mm) of phantom A for an f/1.3 focal configuration. Shear-wave propagation speed can be estimated by evaluating the edge of the wavefront at different times. However, shear attenuation is rather large, thus, normalizing the displacement by its peak value at each time step provides a useful method for visualizing the shear-wave propagation (center). The modulus of phantom A was expected to be 1/3 the magnitude of that of phantom C. (right) Normalized displacement at the focal depth through time in phantom C, a stiffer phantom, for an f/1.3 focal configuration. (The expected ratio of the modulus values is determined by the ratio of the bloom strength of the gelatin for otherwise identical recipes that were used to make the phantoms) (Hall et al. 1997). Note that the inverse of the slope of the lines shown in the center and right-hand images is indicative of the shear wave speed, 1 and 1.7 m/s, respectively. Equation (2) provides corresponding Young's modulus values of 3.0 kPa and 8.7 kPa.

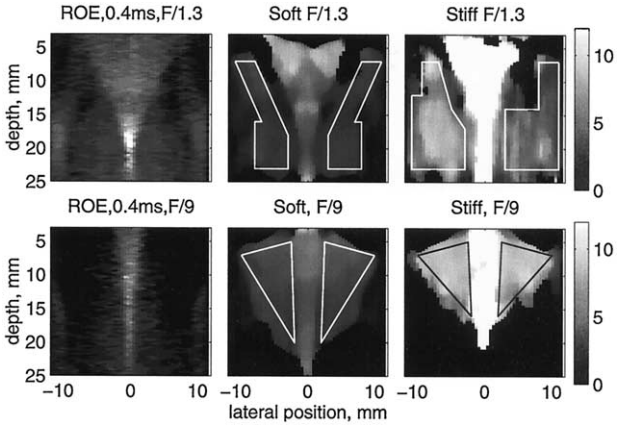

Fig. 3. Reconstructed Young's modulus images from homogeneous phantoms A (center column) and C (right column), using two different focal configurations; top row: f/1.3, 15 mm aperture; bottom row: weakly focused (f/9), 4.4 mm aperture. The ROIs used to compute mean modulus values are outlined in each image. The left-most column presents the normalized displacement 0.4 ms after force cessation in the softer phantom. These two images reflect the spatial extent and magnitude of the applied force (*i.e.,* the ROE) demonstrating the different geometries for the two focal configurations. (upper center) Image of phantom A generated with the same data that are shown in the center image of Fig. 2. The upper right image of phantom C was generated with the same data that is shown in the right-hand image of Fig. 2. (lower center) Image of phantom A generated using a weakly focused (f/9), 4.4-mm aperture. (lower right) Image of phantom C also generated using the weakly focused (f/9), 4.4-mm aperture.

The reconstruction method was implemented on a fresh *ex vivo* breast tissue sample that contained a large fibroadenoma (Fig. 4). An f/1.3 focal configuration was used for this experiment. In this figure, the top row presents matched B-mode and reconstructed modulus images. The left image in the middle row portrays the ROE, with white horizontal lines indicating the depths at which the propagation (*i.e.,* displacement/time wavefront data) is portrayed in the remaining three images (middle right image and bottom row). The mean shear-wave speed of the wavefront moving to the right in these images is 2.0 ± 0.3 and the mean speed of the wavefront moving to the left is 1.0 ± 0.2. This is interesting, because the ROE was completely contained within the fibroadenoma; thus, similar velocities were expected in both directions. These speeds correspond to Young's moduli of 12 and 3 kPa, respectively. The reconstructed Young's modulus image exhibits reasonable agreement of structural boundaries with the matched B-mode image. The fibroadenoma has a higher mean Young's modulus (11.7 ± 3.0 kPa) than the fatty tissue above and to the left (3.8 ± 1.4 kPa). Interestingly, the reconstructed values within the ROE appear to be consistent with those of the surrounding tissue.

In contrast, in the *in vivo* abdomen example (Fig. 5), the reconstructed modulus values within the ROE were variable and have been masked off to facilitate visualization of the tissue structure. An f/1.3 focal configuration was also used in this experiment. In this figure, the top row presents matched B-mode and reconstructed modulus images. The left image in the middle row portrays the ROE, with white horizontal lines indicating the depths at which the propagation (*i.e.,* displacement/time wavefront data) is portrayed in the remaining three images (middle right image and bottom row). The speed of the wavefronts in the middle right image (*i.e.,* the skin) is fairly high, 3.2 ± 0.4 m/s (corresponding to a Young's modulus of 31 kPa). The wavefronts in the bottom images are complex and the slopes of the wavefronts vary with lateral position. The mean Young's moduli portrayed in the upper right image, as determined from solution of eqn (4) (excluding the ROE) are: 14.0 ± 3.8 kPa for skin and 5.6 ± 3.1 kPa for the underlying tissue.

DISCUSSION

The use of acoustic radiation force to generate shear waves remotely was first predicted and demonstrated by Sugimoto et al. (1990) and was more thoroughly treated by Sarvazyan et al. (1998). In their work, a therapeutic transducer was used to generate acoustic radiation force and separate imaging systems were used to observe the

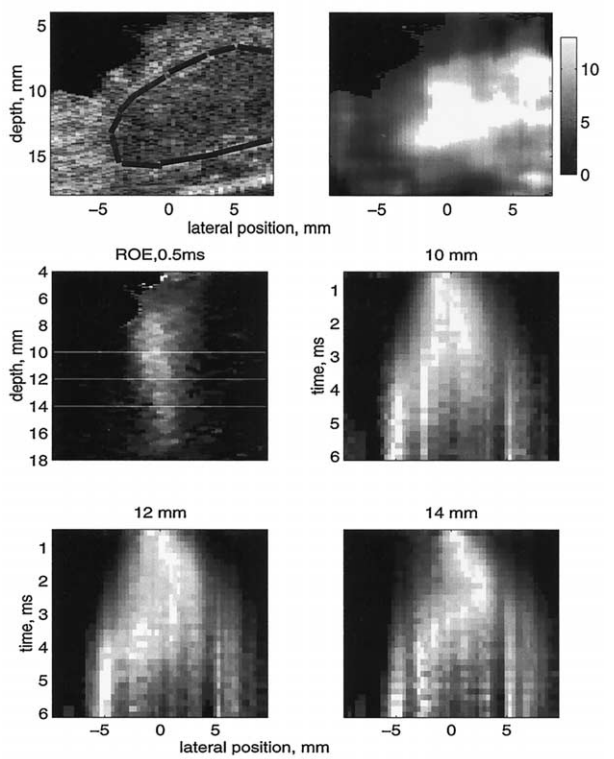

Fig. 4. (top row) Matched B-mode (left) and reconstructed Young's modulus image (right) of an *ex vivo* breast tissue sample. There was a large fibroadenoma on the right side of the tissue sample, outlined in black in the B-mode image and clearly apparent as a region of increased modulus in the reconstructed image. (middle row) 2-D ARFI displacement data immediately after force cessation, indicating the spatial extent of the region of excitation (left) and normalized axial displacement through time at a depth of 10 mm (right). (white horizontal lines) in the ROE image the depths at which the corresponding displacement/time images are displayed. (bottom row) Normalized axial displacement through time at depths of 12 mm (left) and 14 mm (right). Note that the slopes of the wavefronts indicate that the shear wave traveled faster to the right (1.6 m/s) than it did to the left (0.9 m/s). This is misleading, however, because the region of excitation is completely contained within the fibroadenoma. The difference likely occurs due to reflection at the boundary of the fibroadenoma (which occurs on the left side, near −4 mm laterally). The reconstructed image demonstrates consistently higher Young's modulus values throughout the fibroadenoma (even within and to the left of the ROE) and presents reasonable boundary definition.

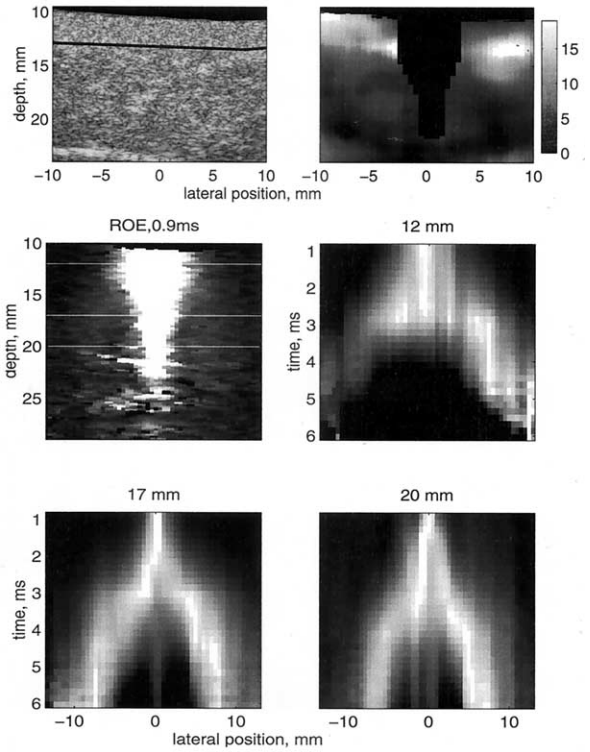

Fig. 5. (top row) Matched B-mode (left) and reconstructed Young's modulus image (right) of an *in vivo* human male abdomen. A stand-off pad was used in this experiment, so the skin ranges from 10 to 13 mm in depth, with the transition from skin to underlying tissue indicated by the black line in the B-mode image. Beneath the skin is presumably fatty tissue. The ROE has been masked off in black in the reconstructed image because the reconstructed values in this region are highly variable and are not considered valid due to the absence of a longitudinal coupling coefficient (λ) in eq. (4) (middle row) 2-D ARFI displacement data immediately after force cessation, indicating the spatial extent of the region of excitation (left) and normalized axial displacement through time at a depth of 12 mm (right). (white horizontal lines) in the ROE image the depths at which the corresponding displacement/time images are displayed. (bottom row) Normalized axial displacement through time at depths of 17 mm (left) and 20 mm (right). Note that the slopes of the wavefronts indicate that the shear wave traveled faster at a depth of 12 mm in the skin than in the underlying fatty tissue. This is consistent with the reconstructed image above (excluding the ROE), indicating a higher Young's modulus in the skin.

resulting shear waves in tissue-mimicking phantoms. In the work presented herein, using a single diagnostic US transducer both to generate acoustic radiation force and image the resulting shear waves, similar behavior was observed near the focal region of the acoustic beam (Fig. 2, left).

In homogeneous media (*i.e.*, the phantoms), the Young's moduli determined by the slope estimation method at the focus are in reasonable agreement with those estimated by the direct inversion method. However, in heterogeneous media, the slope method can be misleading and is not robust. For example, there is an apparent difference in wavefront speed to the left and right within the fibroadenoma (Fig. 4, middle and bottom

rows), and no information is apparent outside its boundaries. This is likely caused by reflection and/or refraction at the boundary of the fibroadenoma at −4 mm laterally. In contrast, the reconstructed Young's modulus image demonstrates a fairly uniform modulus within the fibroadenoma, and the surrounding tissue exhibits a fairly uniform, lower modulus.

One problem with the direct inversion method employed herein is that eqn (3) models only shear propagation, and does not model longitudinal propagation. This is because the Lamé coefficient (λ) that models the coupling between shear and longitudinal waves is not included. Therefore, the reconstructions are not valid within and near the ROE where longitudinal and shear waves interact. In each phantom reconstructed modulus image (Fig. 3), the ROE is clearly apparent as a region of increased magnitude in the shape of the geometric shadow of the active transmit aperture. In the reconstructed abdominal image (Fig. 5), some distortion within the ROE appears to occur; however, in the reconstructed breast tissue image (Fig. 4), distortion is not apparent. These differences might be attributed to differences in the magnitude of the Lamé coefficient, λ, in the different media. Future work will involve derivation of a tractable equation that incorporates this Lamé coefficient. The distortion of information within the ROE differs from our experience with ARFI imaging, where the ROE exhibits the highest SNR, and differences in tissue displacement and recovery portray good agreement with matched B-mode images within the ROE (Nightingale et al. 2002a).

To reduce the size of the ROE one can modify the transmit f-number and/or the transmit frequency of the acoustic beam. Figure 3 provides reconstructed modulus images generated using two different focal configurations in both phantoms A and C. For any shear modulus reconstruction method based upon solution of eqn (3), a narrow region of excitation (*i.e.*, bottom row of Fig. 3) would be beneficial because it allows the largest region of tissue to be reconstructed for a single pushing location. Another advantage of a weakly focused focal configuration is that the direction of shear-wave propagation is primarily lateral and the direction of tissue displacement is primarily axial. This is advantageous because, in our experimental implementation, displacement is only computed in the axial direction.

However, the mean modulus value in both the soft (phantom A) and stiff (phantom C) phantoms is higher for the weakly focused focal configuration (3.8 vs. 2.4 for phantom A and 10.0 vs. 6.8 for phantom C). This is likely due to the assumption that the gradient of displacement in the elevation dimension, the y component of u in eqn (4), is 0. In the transient elastography method, Sandrin et al. (2002), the shear-wave excitation is generated using two parallel rods that create a shear wave where this assumption is valid; however, in ARFI excitation, this is not necessarily true. To accurately quantify the gradient of displacement in the elevation dimension, a 2-D transducer capable of acquiring data over a 3-D volume of tissue would be required for ARFI data. For the existing experimental setup, the validity of neglecting this term differs for the two focal configurations, and leads to an overestimation of the modulus. This suggests that the neglected component might be larger (and, thus, the assumption more problematic) in the f/9 (weakly focused) than in the f/1.3 case. For both focal configurations, phantom C was significantly stiffer than phantom A, with ratios of 2.6 (weakly focused, f/9) and 2.5 (f/1.3). These ratios are reasonably consistent with the expected ratio of 3.0, as determined by the bloom strength ratios of the two phantoms (Hall et al. 1997).

Equation (3) assumes a purely elastic media, neglecting the effects of viscosity. Given that tissue is inherently viscoelastic, this assumption is not accurate. The effect of viscosity would be to introduce a complex shear modulus (and, thus, shear wave speed). The assumption of a real-valued shear modulus likely results in an underestimation of the actual shear-modulus magnitude, which would be greater for tissues demonstrating more viscoelastic behavior. Gelatin-based phantoms have been shown to be fairly elastic Hall et al. 1997; thus, this assumption is likely more problematic in tissues than in our phantoms.

Figures 4 and 5 portray matched B-mode and reconstructed Young's modulus images, as well as normalized shear-wave propagation at different depths in tissue samples *ex vivo* and *in vivo*, respectively. To our knowledge, this is the first demonstration of shear waves generated by acoustic radiation force propagating through tissues. Shear waves clearly propagate through different tissues with different velocities, and the reconstructed modulus images portray reasonable agreement with the matched B-mode images. For example, the fibroadenoma on the right side of the *ex vivo* breast tissue sample (Fig. 4) exhibits higher modulus values than the fatty tissue above and to the left. Quantification of the elastic moduli of soft tissues and tissue-like materials is highly challenging, and the few numbers reported in the literature vary greatly, depending upon measurement method, rate of excitation, applied strain and sample size. Thus, comparison of modulus values seems appropriate only within a given report; however, comparison of trends between reports seems to be reasonable. For example, reported modulus values for normal and diseased breast tissue vary greatly in the literature (1 to 20 kPa for normal breast tissue, and 3 to 100 kPa for breast fibroadenoma) (Skovoroda et al. 1995; Samani et al. 2002; Krouskop et al. 1998). However, a reported trend in the literature is

consistent with that demonstrated herein; breast fibroadenomas have a higher elastic modulus than fatty tissue.

In the *in vivo* example (Fig. 5), the slope of the wavefront in the skin (center right image) corresponds to a higher modulus than that obtained from the direct-inversion method. This might be due to the angle of insonation and wave propagation. The wavefront is tracked along a depth of 12 mm at all lateral locations; however, the transducer was slightly angled with respect to the skin. In addition, different slopes are evident at different lateral locations in the underlying tissue (bottom images). Although the displacement/time wavefronts are useful for visualizing wave propagation, the direct inversion modulus reconstruction method is preferable for 2-D heterogeneous tissue characterization. Using the direct inversion method, the skin demonstrates higher Young's moduli than the underlying fatty tissue (outside of the ROE). We are not aware of another report in the literature quantifying both the moduli of skin and fat. However, intact skin is generally believed to have a higher Young's modulus than fat, as shown in these data.

The direct inversion modulus reconstruction method is challenged in the presence of noise, due to the implementation of the Laplacian and second temporal derivative. Therefore, aggressive filtering was required. This limits the resolution of the resulting images. In addition, to avoid appreciable tissue heating during repeated interrogation of a given location, the amount of energy that can be delivered during each interrogation is reduced from that used in 2-D ARFI imaging. Each pushing interrogation generates approximately 0.2°C (Palmeri et al. 2003) in 2-D ARFI imaging. For shear-wave imaging *in vivo*, the cooling is negligible between interrogations; thus, the heat accumulates and is linearly related to the number of interrogations (Palmeri et al. 2003). Thus, to achieve a 20-mm lateral field of view with spatial sampling on the order of 0.5 mm (*e.g.*, 40 interrogations), the energy in each interrogation must be decreased by approximately 25% to maintain a local temperature increase of less than 6°C. This decreases the resulting tissue displacement magnitudes from those achieved in 2-D ARFI imaging and results in noisier displacement data. Combined with the high attenuation of shear waves in tissues, this presents a considerable challenge for clinical applications of ARFI shear-wave imaging. Even so, the demonstration of *in vivo* feasibility provided by this work supports further investigation.

CONCLUSION

In this paper, we report the first demonstration of *in vivo* and *ex vivo* shear-wave generation from acoustic radiation force. Direct inversion methods were applied to reconstruct the Young's moduli from these data for different tissues and tissue-mimicking phantoms. Mean estimated modulus values for an *ex vivo* breast fibroadenoma and *in vivo* skin were shown to be larger than those for fat. A challenge for ARFI-based shear-wave imaging is presented by the relatively small tissue displacements, which are near the limit of detectability, in combination with the relatively high attenuation of shear waves. This is problematic for direct inversion modulus reconstruction methods, due to the implementation of the Laplacian and second temporal derivative using relatively noisy data. Even so, reasonable agreement between matched structures in the B-mode and reconstructed modulus images was demonstrated in the tissue samples presented.

Acknowledgments—The authors thank Siemens Medical Systems, Ultrasound Group, for their system support. This work was supported by the NIH (grant 8R01EB002132-03) and the Whitaker Foundation.

REFERENCES

Arnett DK, Evans GW, Riley W. Arterial stiffness: A new cardiovascular risk factor? Am J Epidemiol 1994;140:669–682.

Bercoff J, Chaffai S, Tanter M, Fink M. Ultrafast imaging of beamformed shear waves induced by the acoustic radiation force in soft tissues: Application to transient elastography. Proceedings of the 2002 IEEE Ultrasonics Symposium, 2002:1899–1902.

Bilgen M, Insana M. Elastostatics of a spherical inclusion in homogeneous biological media. Phy Med Biol 1998;43(1):1–20.

de Korte C, vander Steen A. Intravascular ultrasound elastography: An overview. Ultrasonics 2002;40:859–865.

D'hooge J, Bijnens B, Thoen J, et al. Echocardiographic strain and strain-rate imaging: A new tool to study regional myocardial function. IEEE Trans Med Imaging 2002;21(9):1022–1030.

Fatemi M, Greenleaf J. Probing the dynamics of tissue at low frequencies with the radiation force of ultrasound. Phys Med Biol 2000; 45(6):1449–1464.

Fu D, Levinson S, Gracewski S, Parker K. Noninvasive quantitative reconstruction of tissue elasticity using an interative forward approach. Phys Med Biol 2000;45(6):1495–1509.

Hall T, Bilgen M, Insana M, Krouskop T. Phantom materials for elastography. IEEE Trans Ultrason Ferroeleo Freq Control 1997; 44(6):1355–1365.

Hall T, Zhu Y, Jaing J, Cook L. Noise reduction strategies in freehand elasticity imaging. Proceedings of the 2002 IEEE Ultrasonics Symposium, 2002:1877–1880.

Krouskop T, Wheeler T, Kallel F, Garra B, Hall T. Elastic moduli of breast and prostate tissues under compression. Ultrason Imaging 1998;20:260–274.

Mai J, Tsou JK, Pellot-Barakat C, et al. Vascular compliance using elasticity imaging. Proceedings of the 2001 IEEE Ultrasonics Symposium, 2001:1577–1580.

McKnight A, Kugel J, Rossman P, et al. Mr elastography of breast cancer: Preliminary results. AJR 2002;178(6):1411–1417.

Muthupillai R, Lomas D, Rossman P, et al. Magnetic resonance elastography by direct visualization of propagating acoustic strain waves. Science 1995;269:1854–1857.

Nightingale K, Bentley R, Trahey G. Observations of tissue response to acoustic radiation force: Opportunities for imaging. Ultrason Imaging 2002a;24:100–108.

Nightingale K, Soo M, Nightingale R, Trahey G. Acoustic radiation force impulse imaging: *In vivo* demonstration of clinical feasibility. Ultrasound Med Biol 2002b;28(2):227–235.

O'Donnell M, Skovoroda A, Shapo B, Emelianov S. Internal displacement and strain imaging using ultrasonic speckle tracking. IEEE Trans Ultrason Ferroelec Freq Control 1994;41:314–325.

Oliphant T, Manduca A, Ehman R, Greenleaf J. Complex-valued stiffness reconstruction from magnetic resonance elastography by algebraic inversion of the differential equation. Magn Reson Med 2001;45:299–310.

Ophir J, Alam S, Garra B, et al. Elastography: Ultrasonic estimation and imaging of the elastic properties of tissue. Proc Inst Mech Eng 1999;213:203–233.

Palmeri M, Trahey G, Nightingale R, Nightingale K. A finite element model of the heating generated during acoustic remote palpation. IEEE Trans Ultrason Ferroelec Freq Control 2003 (in review).

Plewes D, Bishop J, Samani A, Sciarretta J. Visualization and quantification of breast cancer biomechanical properties with magnetic resonance elastography. Phys Med Biol 2000;45(1):1591–1610.

Samani A, Luginbuhl C, Plewes D. Magnetic resonance elastography technique for breast tissue in-vitro elasticity measurement. Proceedings of the 2002 IEEE International Symposium on Biomedical Imaging, 2002:931–934.

Sandrin L, Tanter M, Catheline S, Fink M. Shear modulus imaging with 2-d transient elastography. IEEE Trans Ultrason Ferroelec Freq Control 2002;49(4):426–435.

Sarvazyan A, Rudenko O, Swanson S, Fowlkes J, Emelianov S. Shear wave elasticity imaging: A new ultrasonic technology of medical diagnostics. Ultrasound Med Biol 1998;24(9):1419–1435.

Sinkus R, Lorenzen J, Schrader D, et al. High-resolution tensor mr elastography for breast tumour detection. Phys Med Biol 2000; 45(6):1649–1664.

Skovoroda A, Klishko A, Gusakyan D, et al. Quantitative analysis of the mechanical characteristics of pathologically changed soft biological tissues. Biophysics 1995;40(6):1359–1364.

Steele D, Chenevert T, Skovoroda A, Emelianov S. Three-dimensional static displacement, stimulated echo NMR elasticity imaging. Phys Med Biol 2000;45(1):1633–1648.

Sugimoto T, Ueha S, Itoh K. Tissue hardness measurement using the radiation force of focused ultrasound. Proceedings of the 1990 IEEE Ultrasonics Symposium, 1990;1377–1380.

Taylor L, Porter B, Rubens D, Parker K. Three-dimensional sonoelastography: Principles and practices. Phys Med Biol 2000;45:1477–1494.

Trahey G, Allison J, Von Ramm O. Angle independent ultrasonic detection of blood flow. IEEE Trans Biomed Engr 1987;BME-34(12):965–967.

Van Houten E, Weaver J, Miga M, Kennedy F, Paulsen K. Elasticity reconstruction from experimental mr displacement data: Initial experience with an overlapping subzone finite element inversion process. Med Phys 2000;27(1):101–107.

Varghese T, Zagzebski J, Rahko P, et al. Ultrasonic imaging of myocardial strain using cardiac elastography. Ultrason Imaging 2003; 25(1):1–16.

Walker W, Fernandez F, Negron L. A method of imaging viscoelastic parameters with acoustic radiation force. Phys Med Biol 2000; 45(6):1437–1447.

Zhu Y, Chaturvedi P, Insana M. Strain imaging with a deformable mesh. Ultrason Imaging 1999;21(2):127–146.